Diatomic Catalysts for Fenton and Fenton-like Reactions: New Advances and In-Depth Insights

Fan Mo, Qixing Zhou[*], Chenghao Li, Zongxin Tao, Zelin Hou, Tong Zheng, Qi Wang, Shaohu Ouyang, Sihui Zhan

Key Laboratory of Pollution Processes and Environmental Criteria (Ministry of Education)/Tianjin Key Laboratory of Environmental Remediation and Pollution Control, Carbon Neutrality Interdisciplinary Science Center, College of Environmental Science and Engineering, Nankai University, Tianjin 300350, China.

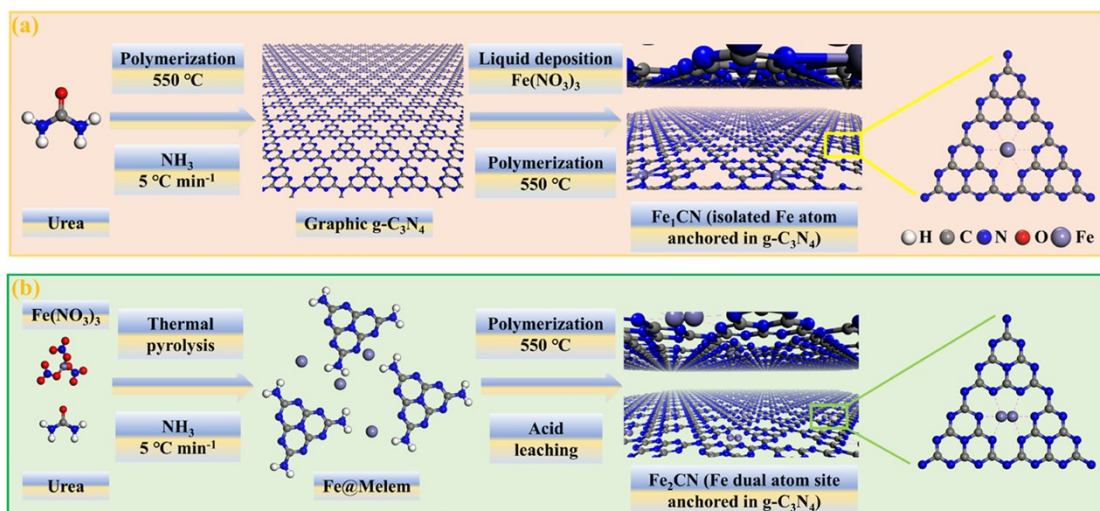To whom correspondence may be addressed. Email: zhouqx@nankai.edu.cn (Q. Zhou).

Fig. S1. Critical synthesis process for (a) Fe$_1$CN and (b) Fe$_2$CN. Reprinted (adapted) with permission from (1). Copyright 2022 ACS.
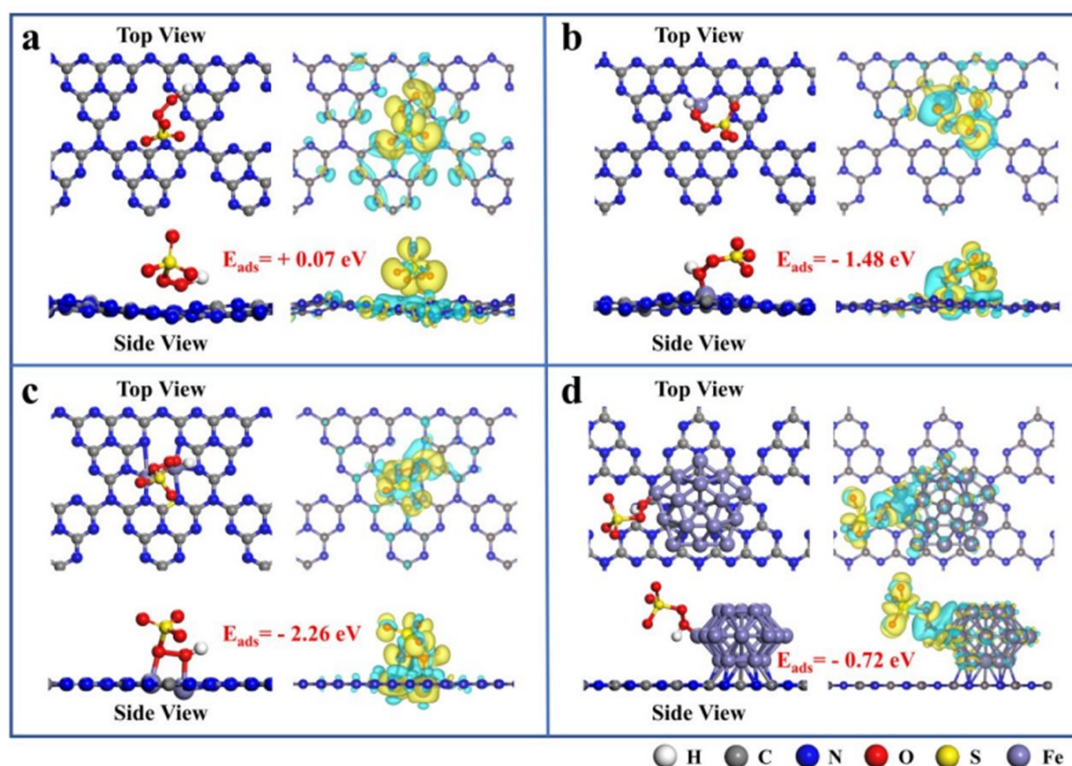

Fig. S2. The adsorption configuration and the charge density difference of PMS adsorbed on (a) g-C$_3$N$_4$, (b) Fe$_1$CN, (c) Fe$_2$CN, and (d) Fe$_n$CN. The light yellow and light blue isosurfaces represent electron accumulation and depletion, respectively. Reprinted (adapted) with permission from (1). Copyright 2022 ACS.
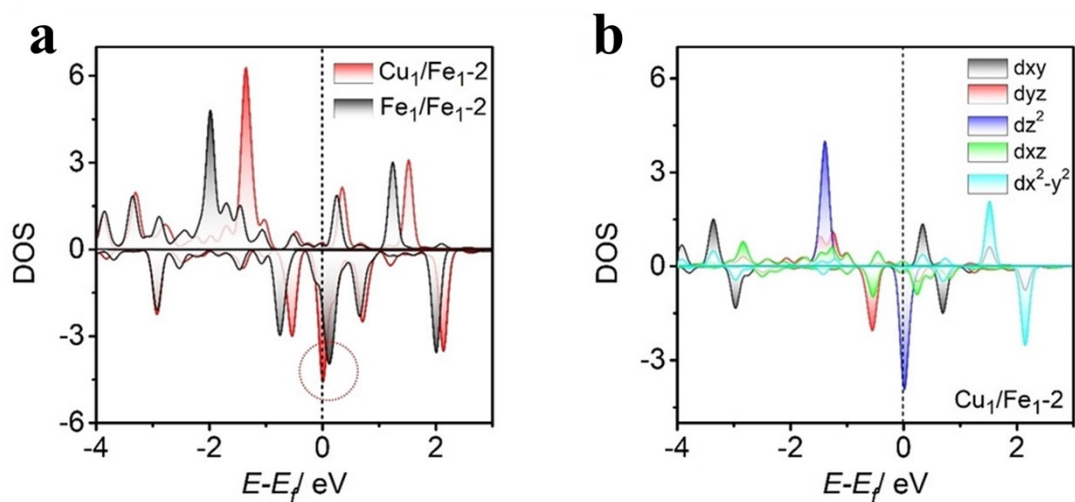
Fig. S3. (a) Fe 3d DOS of Fe_1/Fe_1-2 and Cu_1/Fe_1-2. (b) DOS of the five Fe 3d orbitals in Cu_1/Fe_1-2. Reprinted (adapted) with permission from (2). Copyright 2022 ACS.
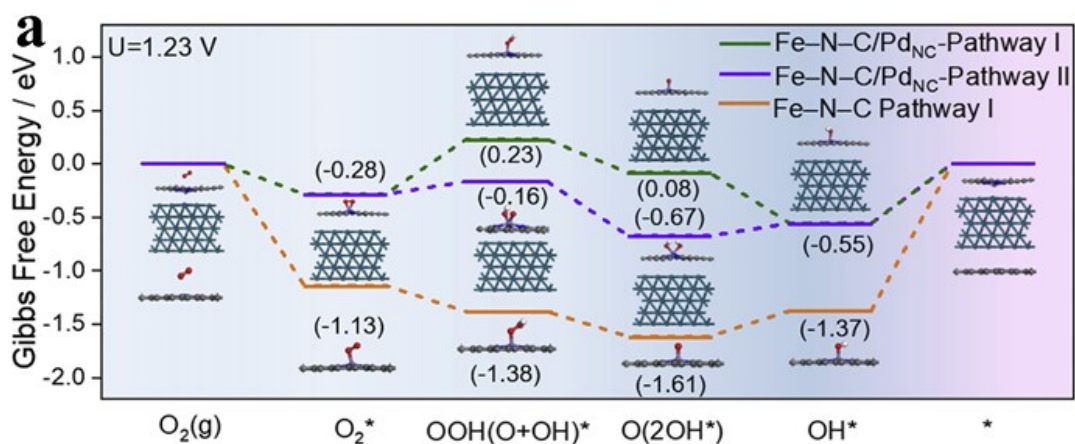

Fig. S4 (Corresponding to Fig. 3a). (a) Gibbs free energy diagram of ORR after the consideration of solvent effect. Reprinted (adapted) with permission from (3). Copyright 2022 Cell Press.
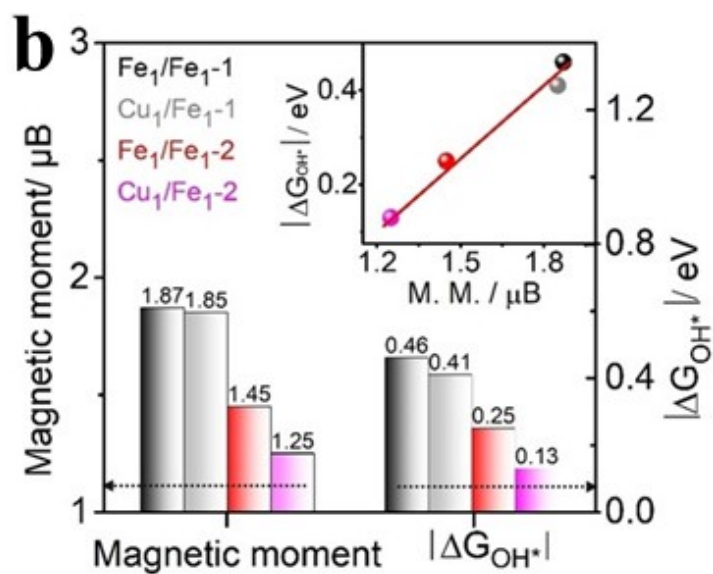
Fig. S5 (Corresponding to Fig. 3b). Comparison of magnetic moment and ΔG_{OH*}. Reprinted (adapted) with permission from (2). Copyright 2022 Wiley.
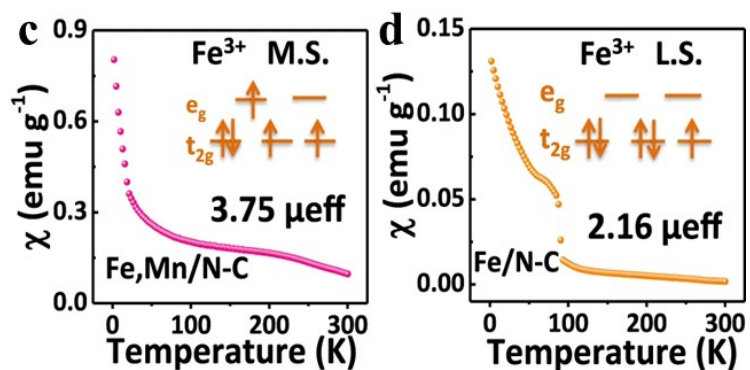

Fig. S6 (corresponding to Fig. 3c and d). Magnetic susceptibility of (c) Fe-Mn/NC, (d) Fe/NC (M.S. represents medium-spin, L.S. represents low-spin), with permission from (4) copyright 2021 Springer Nature.
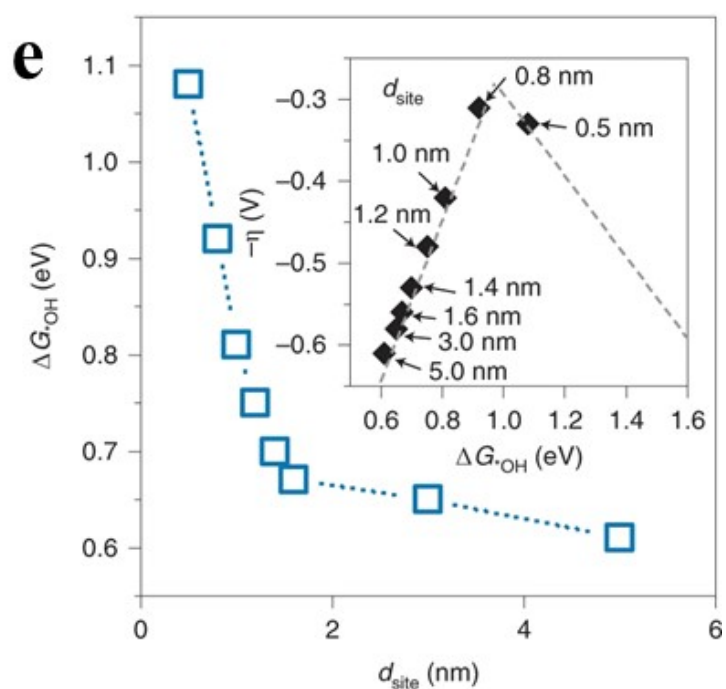
Fig. S7 (corresponding to Fig. 3e). The d_{site}-dependent ΔG_{OH*} obtained by DFT calculations. Inset: volcano plot of calculated overpotentials for the ORR against ΔG_{OH*}. Reprinted (adapted) with permission from (5). Copyright 2021 Springer Nature.
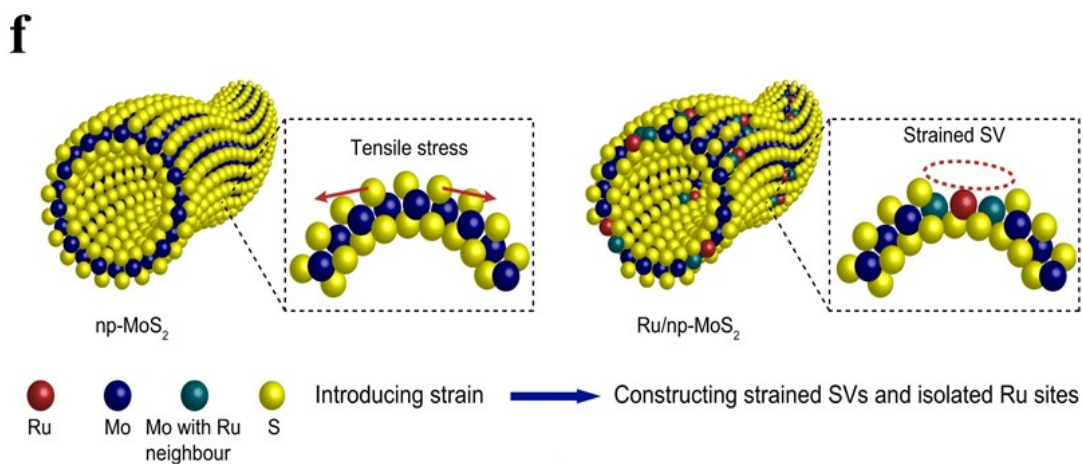

Fig. S8 (corresponding to Fig. 3f). Illustration of the construction Ru/np-MoS$_2$. Reprinted (adapted) with permission from (6). Copyright 2021 Springer Nature.
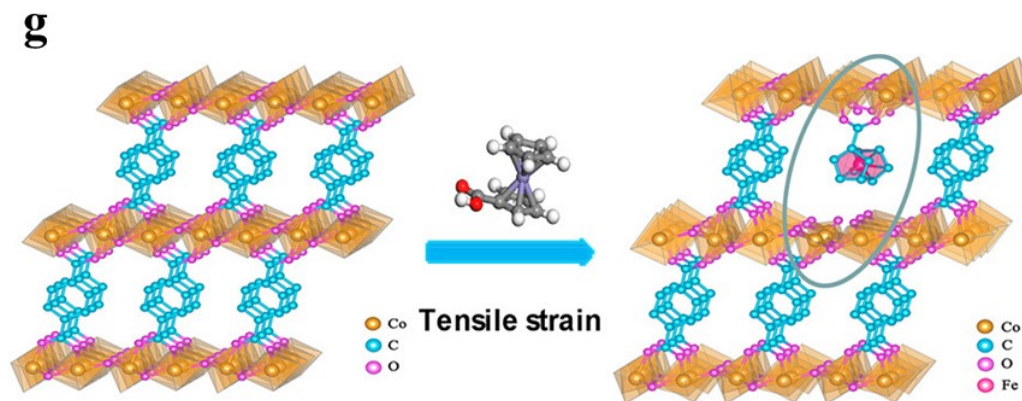
Fig. S9 (corresponding to Fig. 3g). (g) Crystal structures of CoBDC and CoBDC FcCA models obtained from DFT simulations. The microreactor composed of directly coordinated with carboxyl oxygen atom of FcCA (Co1), unsaturated coordinative Co2, together with FcCA linker labeled by circle. Reprinted (adapted) with permission from (7). Copyright 2021 ACS.
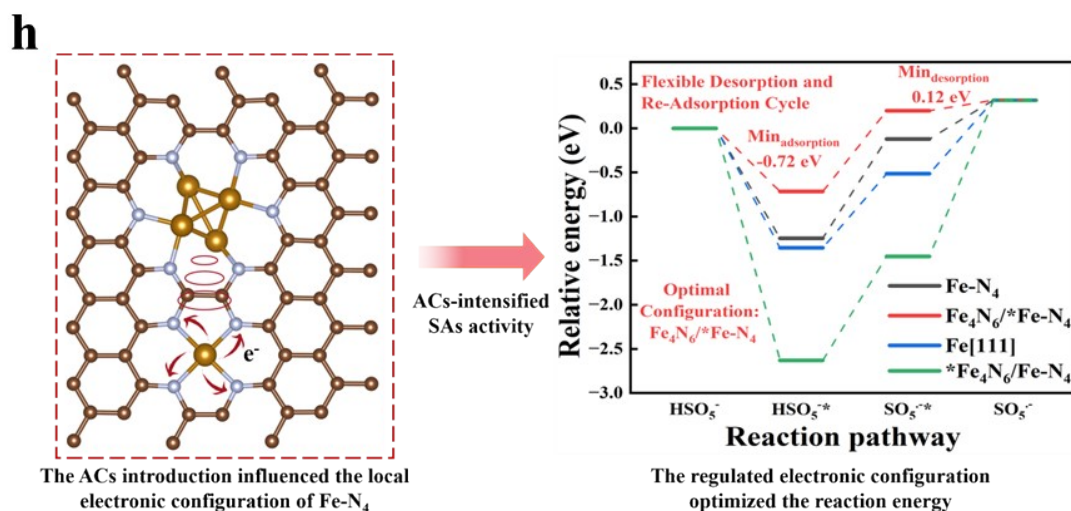

Fig. S10 (corresponding to Fig. 3h). The regulatory role of Fe ACs on the Fe SAs-mediated PMS oxidation reaction. Reprinted (adapted) with permission from (8). Copyright 2023 PNAS.
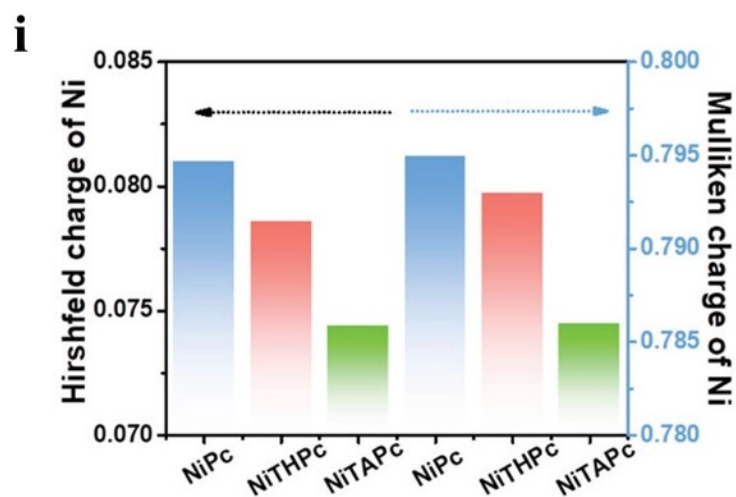
Fig. S11 (corresponding to Fig. 3i). (i) Hirshfeld and Mulliken charges of Ni atom in NiPc, NiTHPc, and NiTAPc. Reprinted (adapted) with permission from (9). Copyright 2021 Wiley.
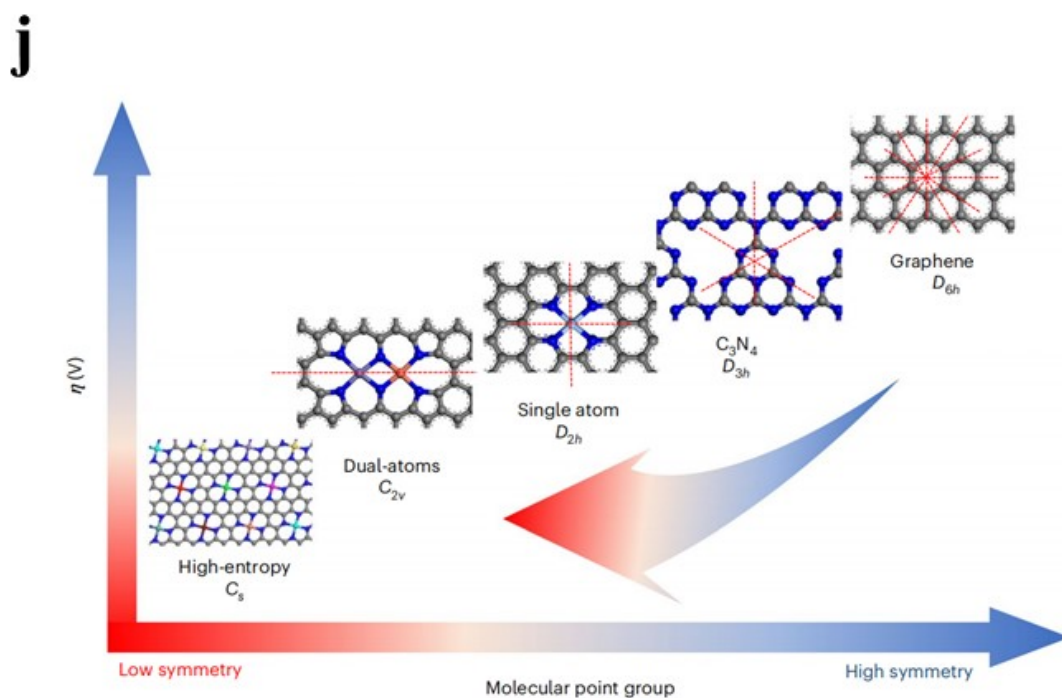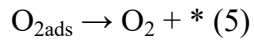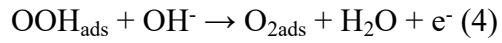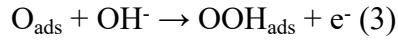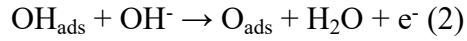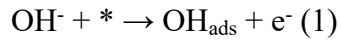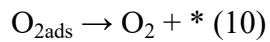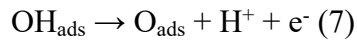

Fig. S12 (corresponding to Fig. 3j). (j) The relationship between symmetry and electrocatalytic performance, with permission from (10) copyright 2023 Springer Nature.

Equation

OER in alkaline solution (ORR is the reverse reaction of OER)

$OH^- + * \rightarrow OH_{ads} + e^-$ (1)

$OH_{ads} + OH^- \rightarrow O_{ads} + H_2O + e^-$ (2)

$O_{ads} + OH^- \rightarrow OOH_{ads} + e^-$ (3)

$OOH_{ads} + OH^- \rightarrow O_{2ads} + H_2O + e^-$ (4)

$O_{2ads} \rightarrow O_2 + *$ (5)

OER in acidic solution (ORR is the reverse reaction of OER)

$H_2O + * \rightarrow OH_{ads} + H^+ + e^-$ (6)

$OH_{ads} \rightarrow O_{ads} + H^+ + e^-$ (7)

$O_{ads} + H_2O \rightarrow OOH_{ads} + H^+ + e^-$ (8)

$OOH_{ads} \rightarrow O_{2ads} + H^+ + e^-$ (9)

$O_{2ads} \rightarrow O_2 + *$ (10)

HER in alkaline solution

$H_2O + e^- \rightarrow OH^- + H_{ads}$ (Volmer) (11)

$H_{ads} + H_2O + e^- \rightarrow OH^- + H_2$ (Heyrovsky) (12)

or $2H_{ads} \rightarrow H_2$ (Tafel) (13)

HER in acidic solution

$H^+ + e^- + * \rightarrow H_{ads}$ (Volmer) (14)

$H_{ads} + H^+ + e^- \rightarrow H_2$ (Heyrovsky) (15)

or $2H_{ads} \rightarrow H_2$ (Tafel) (16)
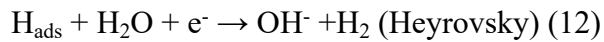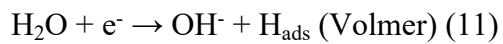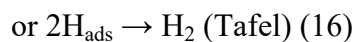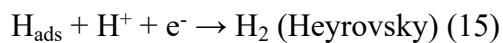
References

1. J. Li *et al.*, Modulating the electronic coordination configuration and d-band center in homo-diatomic Fe_2N_6 catalysts for enhanced peroxymonosulfate activation. *ACS Appl. Mater. Interfaces* **14**, 37865-37877 (2022).

2. T. He *et al.*, Theory-guided regulation of FeN_4 spin state by neighboring Cu atoms for enhanced oxygen reduction electrocatalysis in flexible metal–air batteries. *Angew. Chem., Int. Ed. Engl.* **134**, e202201007 (2022).

3. X. Wei *et al.*, Tuning the spin state of Fe single atoms by Pd nanoclusters enables robust oxygen reduction with dissociative pathway. *Chem* **9**, 181-197 (2023).

4. G. Yang *et al.*, Regulating Fe-spin state by atomically dispersed Mn-N in Fe-N-C catalysts with high oxygen reduction activity. *Nat. Commun.* **12**, 1734 (2021).

5. Z. Jin *et al.*, Understanding the inter-site distance effect in single-atom catalysts for oxygen electroreduction. *Nat. Catal.* **4**, 615-622 (2021).

6. K. Jiang *et al.*, Rational strain engineering of single-atom ruthenium on nanoporous MoS(2) for highly efficient hydrogen evolution. *Nat. Commun.* **12**, 1687 (2021).

7. F. He *et al.*, Metal-organic frameworks with assembled bifunctional microreactor for charge modulation and strain generation toward enhanced oxygen electrocatalysis. *ACS Nano* **16**, 9523-9534 (2022).

8. F. Mo *et al.*, The optimized Fenton-like activity of Fe single-atom sites by Fe atomic clusters-mediated electronic configuration modulation. *Proc. Natl. Acad. Sci. U. S. A.* **120**, e2300281120 (2023).

9. K. Chen *et al.*, Ligand engineering in nickel phthalocyanine to boost the electrocatalytic reduction of CO_2. *Adv. Funct. Mater.* **32**, 2111322 (2021).

10. X. Lei *et al.*, High-entropy single-atom activated carbon catalysts for sustainable oxygen electrocatalysis. *Nat. Sustain.* 10.1038/s41893-023-01101-z (2023).